Short-range ordering effects on the electronic Bloch spectral function of real materials in the nonlocal coherent-potential approximation

Alberto Marmodoro,[1,2,*] Arthur Ernst,[1] Sergei Ostanin,[1] Leonid Sandratskii,[1] Paolo E. Trevisanutto,[3,4] Nektarios N. Lathiotakis,[5] and Julie B. Staunton[6]

[1]*Max-Planck-Institut für Mikrostrukturphysik, Weinberg 2, D-6120 Halle, Germany*

[2]*Institut für Theoretische Physik, Goethe-Universität Frankfurt am Main, Max-von-Laue-Strasse 1, 60438 Frankfurt am Main, Germany*

[3]*Singapore Synchrotron Light Source, National University of Singapore, 5 Research Link, Singapore 117603*

[4]*Singapore Centre for Advanced 2D Materials and Graphene Reseach Centre, National University of Singapore, Singapore, 117546*

[5]*Theoretical and Physical Chemistry Institute, National Hellenic Research Foundation, Vass. Constantinou 48, GR-11635 Athens, Greece*

[6]*University of Warwick, Department of Physics, Coventry CV4 7AL, United Kingdom*

(Received 24 August 2016; revised manuscript received 19 November 2016; published 21 December 2016)

The nonlocal coherent-potential approximation provides a systematic technique for the study of short-range ordering effects in a variety of disordered systems. In its original formulation the technique, however, shows an unwanted dependence on details in the coarse-grained effective medium construction. This is particularly evident in the study of $\vec{k}$-resolved quantities, such as the Bloch spectral function and other non-site-diagonal observables. We remove the issue and recover fully physical results in first principles studies of real materials, by means of a resampling procedure first proposed for model tight-binding Hamiltonians. The prescription is further generalized to the case of complex unit cell compounds, with more than a single sublattice, and illustrated through examples from metallic alloys and disordered local moment simulations of paramagnetism in the prototype iron-based superconductor FeSe.

DOI: 10.1103/PhysRevB.94.224205

I. INTRODUCTION

First principles studies of solid state systems take great advantage from exploitation of all symmetries that can be present in a compound. Among these, idealized lattice periodicity is often crucial to make the problem numerically tractable. Most real materials, however, are disordered to some extent, making this simplification in principle unavailable. Alloys, for example, possess substitutional disorder, magnetic metals at finite temperature show the effects of local moment disorder, and thermally induced atomic displacements from equilibrium lattice positions can also fall in the same general picture [1]. Strong electronic correlations and other many body effects can bring in further complications of a related kind.

Much effort has been devoted to devising approximation schemes suited to the extra challenges presented by such scenarios. In general, the different approaches can be classified into either supercell or effective medium frameworks. The latter class can be attractive owing in particular to the lack of rapidly increasingly computational costs, while producing a solution which restores translational invariance on the primitive unit cell scale. In this context, the coherent potential approximation (CPA) [2] provides a sophisticated and well-established solution scheme, which has been rigorously evaluated at a theoretical level as well as having been successfully put to the test in many applications.

Similar to dynamical mean free theory (DMFT) for strongly correlated electron systems [3,4], the method owes much of its power to the construction of an energy-dependent effective medium that captures the essence of the actual compound on the average. Only a fraction of the computational cost, which would be required to explicitly investigate a big enough portion of the sample with respect to assigned concentration of "impurities," is then needed. This is accomplished by determining self-consistently a solution at every energy of interest, down to the desired no extra scattering threshold. Consistency of any error thus introduced, together with restoration of on-average lattice periodicity, allows then to port over at small increase of complexity the practical formulation of how to compute a variety of observables from their long-range ordered (LRO) expressions.

Combined with density functional theory (DFT) and Kohn-Korringa-Rostoker (KKR) multiple scattering theory [5–7], the CPA can produce an accurate *ab initio* description of disordered systems which has been successfully deployed for many applications. It is however in essence a single-site mean field theory and as such unable to address short-range order (SRO) effects. Only the average concentration enters the scheme as input, clearly restricting the ability to feed the algorithm with additional experimental or theoretical insights concerning all sorts of local environment effects and short-ranged impurity correlations.

Among the several proposals to eliminate this limitation from the CPA, the nonlocal CPA (NLCPA) derived by Rowlands *et al.* [8] from Jarrell's *et al.* [9] dynamical cluster approximation (DCA) follows a coupled direct space—reciprocal space reworking of the original theory. In this development the constraint of a single-site concentration is removed, to give access to the full statistics of an enlarged, multisite cavity. This consists of N_c instances of the original $N_{\mathrm{sub}} \geqslant 1$ sublattices unit cell, in which for a disordered system different atomic species are allowed to appear in various arrangements, according to a given probability distribution. All forms of local correlation and short-range ordering (SRO) can then be set up within the spatial extent of the cavity. On the other hand other desirable features of the general method are retained, such as translational invariance in the effective

*amarmodo@mpi-halle.mpg.de

medium (as opposed to other CPA extension proposals such as for instance the molecular CPA [10,11]). This is a result of consistently carrying through from the above enlarged cluster treatment in direct space the implication of a coarse-grained Brillouin zone $\mathbf{\Omega}_{\mathrm{BZ}}$ in reciprocal space, which is sampled over the same number N_c of nonoverlapping tiles labeled by so-called "cluster momenta" [8] $\vec{K}_n$. The effective medium therefore retains the same amount of information in either representation, while iterating back and forth via repeated lattice Fourier transforms until convergence.

Pioneering works on the NLCPA have initially followed the route traced by the earlier single-site CPA developments. The basic ideas have been tested with model, tight-binding Hamiltonians [8], where results in terms of simple observables such as the electronic density of states (DOS) could also be checked through exhaustive numerics. In the form suited for detailed *ab initio* work, the KKR-NLCPA has been applied to studies of the DOS of simple unit cell metallic alloys [12] and has then been fully implemented at a self-consistent field (SCF)-DFT level [13]. Further work is ongoing to incorporate it into calculations of the full Gibbs' free energy for phase diagram investigations [14–16]. In parallel with this, another line of development has examined the more general case of transport in linear response [17,18] and non-site-diagonal observables [19–21] in disordered systems, the first example of which is given by the Bloch spectral function [22] (BSF) which is the main subject of this paper. This quantity can also be related to mean-free-path-based model treatments of conductivity, through extraction of the relevant parameters from Lorentzian fits [23].

From these latter efforts a new aspect of the NLCPA has progressively emerged. While the single-site version of the CPA leaves no room for arbitrariness, it has been recently realized that the extension of the direct space cavity to span $N_c \geqslant 1$ times the volume of the original single-site CPA model, and the subsequent retention of a conversely more finely coarse-grained effective medium to account for associated SRO effects, together expose DCA/NLCPA results to severe dependence on a free phase choice in the adoption of lattice Fourier transformations used to pursue self-consistency. Correspondingly, observables such as the BSF exhibit artifacts in the form of abrupt, unphysical discontinuities upon crossing boundaries between the N_c different coarse-grained regions, into which the Brillouin zone has been tiled (Fig. 1).

This point is briefly reviewed in Sec. II below, and a recent proposal [24] on how to amend the scheme is here put to the first concrete test in its KKR level deployment for real materials (Sec. II B). We also address a somewhat less intuitive but still rather fundamental gap in the framework, examining how the above concepts transfer to $N_{\mathrm{sub}} > 1$ studies where no Brillouin zone tiling is used (i.e., $N_c = 1$), but SRO sensitivity is retained in the form of intersublattice corrections within the cavity.

In such a case it has first been shown, again in models [25] as well as full SCF-DFT KKR implementations of the scheme [26], how the corresponding effective medium leads to identical site-diagonal observables such as the DOS, in the limit of appropriate test cases. Simple examples for this testing have been a $N_{\mathrm{sub}} = 2$, $N_c = 1$ CsCl-like unit cell, with both

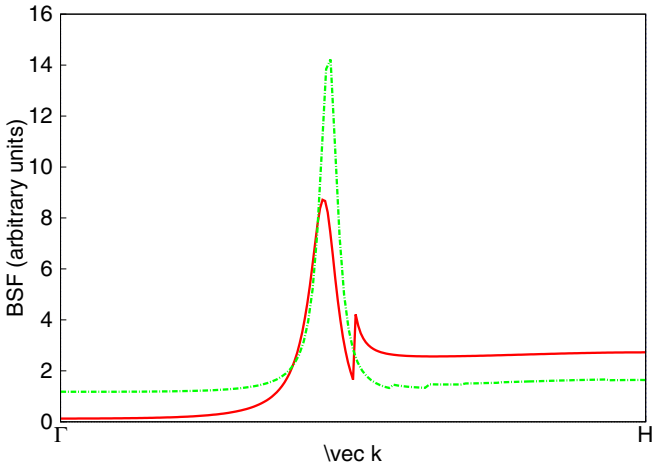

FIG. 1. Single energy point evaluation of the BSF for *bcc* CuZn, examined for $SRO = +1$ within a $N_c = 2$, $N_{\mathrm{sub}} = 1$ NLCPA cavity for the single tiling phase choice $\vec{\phi} = (0,0,0)$ (red) and after the tiling phase average of Eq. (12) (green). Continuity is recovered as a function of the resampling N_p.

positions occupied either by Cu or Zn, that hence realize the same physics as a $N_{\mathrm{sub}} = 1$ *bcc* alloy studied for $N_c = 2$; or similarly, a $N_{\mathrm{sub}} = 4$, $N_c = 1$ Cu_3Au-like unit cell, compared with a *fcc* $N_{\mathrm{sub}} = 1$ *fcc* alloy with $N_c = 4$ setup. Since the choice among descriptions is in the above cases fully arbitrary, physical results should also be consistent across it. Particularly from the point of view of non-site-diagonal (NSD) observables however, the counterpart of coarse-graining tiles boundaries is less intuitive when $N_c = 1$, and no obvious splitting within the Brillouin zone is in use to possibly give rise to discontinuities in $\vec{k}$-resolved observables such as the BSF. Truncation to a finite cavity size in direct space, and free phase freedom in the lattice Fourier transformation, are however still present; and again a complete formalism should lead to equivalence in results regardless of the chosen representation for the problem. We address this aspect of the theory in Sec. II C and show how the above resampling idea carries over to this side of the multisublattice NLCPA.

The above theory extensions are showcased through the illustrative example of a ferromagnetic $Fe_{0.75}$,$Pd_{0.25}$ alloy in the presence of substitutional SRO (Sec. III B), focusing attention in particular on the minority spin channel for which the BSF is most affected by the average local environment of either Fe or Pd atoms. As a second illustration, we also examine a disordered local moment (DLM) treatment [27–30] for the highly topical example of paramagnetism in FeSe (Sec. III C). We draw some overall conclusions in Sec. IV.

II. THEORY OVERVIEW

We recall that for a perfectly ordered solid the BSF can be written as:

$$A_B(\vec{k},E) = \sum_n \delta(E - \varepsilon_n(\vec{k})), \tag{1}$$

where $\varepsilon_n(\vec{k})$ are energy eigenvalues defining the band structure of the system as a series of infinitely sharp peaks. For a

disordered material with random lattice sites' occupancy, but still periodic spatial arrangement of atomic positions, the BSF can be defined as the Fourier transform of the site off-diagonal, configurationally averaged Green function $\langle G(\vec{r},\vec{r}',E)\rangle$:

$$\overline{A}_B(\vec{k},E) = -\frac{1}{\pi}\Im\sum_j\sum_{s'=1}^{N_{\rm sub}}\int_{\mathbf{\Omega}(\vec{R}_j+\vec{b}_{s'})}\mathrm{Tr}\langle\underline{G}(\vec{r},\vec{r}+\vec{b}_{s'} + \vec{R}_j,E)\rangle d\vec{r}\, e^{-i\vec{k}\cdot\vec{R}_j}, \quad (2)$$

where $\vec{R}_j$ represents a unit cell lattice vector with $j = 1,\ldots,\infty$ in the macroscopic limit, $\vec{b}_{s'}$ denotes the position of a site on sublattice s' from such origin, and $\vec{r}$ is a vector within the surrounding region $\mathbf{\Omega}(\vec{R}_j+\vec{b}_{s'})$ so that $\vec{\bar{r}} = \vec{R}_j+\vec{b}_{s'}+\vec{r}$. An underline indicates that the propagator has been expanded in matrix form over composite angular momentum indices $L = (\ell,m) = \ell^*(\ell+1)+m+1$.

The CPA provides an efficient method to compute such a quantity. We recall here only essential aspects of the formalism and refer to Refs. [11,19,22] for more comprehensive reviews. Its fundamental assumptions derive from experimental evidence that periodicity in a material's lattice geometry can persist, even if occupation of any atomic site $\vec{R}_j$ by a certain chemical species is only assigned in a statistical sense due to disorder.

This suggests considering building up a description, as if each crystallographic position would be periodically occupied by a fictitious, intermediate scattering potential. This corresponds in some sense to an average between all alternative $N_{alt} \geqslant 1$ atomic species which can randomly appear on a particular, arbitrary site. This goal is in particular pursued in a dynamic, i.e., energy-dependent fashion, demanding in KKR language that electrons shall not incur, on average, into extra scattering throughout any local portion of the system [31,32].

The (multisublattice) nonlocal extension of the theory follows on top of this premise, using the seminal insight from the dynamic mean field approximation work of Müller-Hartmann [33] and Jarrell [9]. Its goal is to improve the above picture with the inclusion of local environment effects. To accomplish the task, a larger-than-single-site portion of the sample, or "cavity" [8,10,26], is considered in direct space. Different forms of disorder and SRO can then be simply set up through assignment of $N_{\rm tot}$ different probabilistic weight to all ways to populate such $N_c \times N_{\rm sub} \geqslant 1$ lattice sites, at positions $\vec{R}_I+\vec{b}_s$, with $I = 1,2,\ldots,N_c$ and $s = 1,2,\ldots,N_{\rm sub}$.

If we denote as γ each possible configuration of atomic potential α's occurring on such a lattice site within the cavity, $\{\alpha_{1,1},\ldots,\alpha_{I,s},\ldots,\alpha_{N_c,N_{\rm sub}}\}$, we have in general $N_{\rm tot} = \prod_{s=1}^{N_{\rm sub}} N_{alt}^{N_c}(s)$ of these. By assigning to every configuration γ the desired probabilistic weight $P(\gamma)$, where $P(\gamma)\in[0,100\%]$ and $\sum_{\gamma=1}^{N_{\rm tot}} P(\gamma) = 100\%$, the formalism allows different SRO regimes to be simulated, from fully uncorrelated to long-range ordered (LRO), i.e., fully periodic scenarios.

This input goes back to the single-site version of the theory (or its complex unit cell generalization (MSCPA) by Pindor *et al.* [34]), when the above probability distribution is chosen to be simply the product of local concentrations alone [8,26]. Conversely, the treatment becomes exact but specific to a single, perfectly repeating realization of the lattice (as in a supercell treatment) in the opposite limit where $N_c \times N_{\rm sub}$ is enlarged to mimic the full sample, but gets populated with a single configuration γ_1 with $P(\gamma_1) = 100\%$.

Details concerning the self-consistent construction of the NLCPA effective medium solution from the above starting point can be found in Refs. [8,11,13,25,26] and will not be repeated here. In the following we focus instead on one additional aspect of such converged solutions, peculiar to the DCA/NLCPA as opposed to less stringent "cluster DMFT"/"cluster CPA" extension proposals in the literature. While initially not particularly remarked upon, its importance stands out very clearly, as soon as the original scheme gets deployed for NSD observables that represent the most general context of applications. We recall with this classification Faulkner and Stocks' original conceptual framework [19], which distinguishes such effective medium quantities from site-diagonal (SD) ones by considering whether their definition requires "averaging" contributions from two sites $\vec{R}_i+\vec{b}_s$, $\vec{R}_j+\vec{b}_{s'}$ (with i, j labeling arbitrarily distant unit cells within the bulk, as needed as the $\vec{k}$ resolution increases) or just one unit cell at the time. The simplest example of the former case is offered by the BSF $\overline{A}(\vec{k},E)$ of Eq. (2), in its nature as the Fourier transformed imaginary part of the electronic propagator $\overline{G}(\vec{R}_j+\vec{b}_{s'},\vec{R}_i+\vec{b}_s,E)$. To the latter SD category belongs instead, for instance, the electronic density of states $\overline{n}(E)$.

Clearly NSD quantities have the ability to pick up and express more structure in the effective medium. We note however how, although further integration of the full NSD expression for a given observable returns the corresponding SD counterpart (such as in the case of the DOS upon integrating the BSF over all $\vec{k}\in\mathbf{\Omega}_{\rm BZ}$), a simplified version of the CPA Green function expression is in practice sufficient when one intends to compute only SD observables. A typical example is the effective medium electronic charge, as needed for full SCF-DFT implementations of the (NL)CPA [12,13,16,26].

In the case of the BSF $\overline{A}(\vec{k},E)$, Faulkner and Stocks could in fact show [19] how application of the so-called "Lax's approximation" [35,36] on top of the single-site CPA effective medium leads to a complete formula for the Green function at any $\vec{k}\in\mathbf{\Omega}_{\rm BZ}$ and complex energy $z = E+i\eta$ ($\eta\geqslant 0$) that contains most generally three terms [19]:

$$\overline{\underline{G}}(\vec{k},z) = \overline{\underline{G}}^{(\rm SD)}(z) - \overline{\underline{G}}^{(\rm NSD)}(z) + \overline{\underline{G}}^{(\rm NSD)}(\vec{k},z). \quad (3)$$

One can see in particular how a mutual cancellation between first and second terms takes place in the LRO limit, i.e., in the absence of disorder, and between the second and third term instead in the SD limit, i.e., when considering the effective medium electronic propagator only within a single unit cell, as sufficient, i.e., for the DOS.

Upon porting the same argument to the $N_c \geqslant 1$-wide NLCPA cavity, limited at first only to $N_{\rm sub} = 1$ systems, Tulip *et al.* [22] have also come to a similar conclusion, which we give concisely and together with complex unit cell extension as:

$$\overline{\underline{\underline{G}}}(\vec{k},z) = \overline{\underline{\underline{G}}}^{(\rm CD)}(z) - \overline{\underline{\underline{G}}}^{(\rm NCD)}(z) + \overline{\underline{\underline{G}}}^{(\rm NCD)}(\vec{k},z) \quad (4)$$

(where additional underlines to denote matrices in $I,J = 1,\ldots,N_c$ and s,s' sublattice indices, and the different terms

now refer to cavity-diagonal (CD) or non-cavity-diagonal (NCD) contributions). Introducing for convenience the notation: $[\underline{A}\,\underline{B}]_{i,j} = \sum_k A_{i,k}B_{k,j}$ for row-column products between matrices $\underline{A},\underline{B}$, $[\underline{A}\odot\underline{B}]_{i,j} = A_{i,j}B_{i,j}$ for direct, entry-by-entry products, $\underline{\underline{1}}$ for the identity matrix, we can define the NLCPA cavity-extended "impurity projector" matrices already used by the original theory [19]:

$$\underline{\underline{D}}^{(\gamma)}(z) = (\underline{\underline{1}} + \underline{\underline{\overline{t}}}(z)(\underline{\underline{m}}^{(\gamma)}(z) - \underline{\underline{\overline{m}}}(z)))^{-1} \tag{5}$$

with $\underline{\underline{m}}^{(\gamma)}(z) = (\underline{\underline{t}}^{(\gamma)}(z))^{-1}$, $\underline{\underline{\overline{m}}}(z) = (\underline{\underline{\overline{t}}}(z))^{-1}$.

Similarly, we also extend over N_c and $N_{\rm sub}$ the integrals of products between regular (irregular) radial solutions [19] $Z_L^{(\alpha(I,s,\gamma))}(z)$, $(J_L^{(\alpha(I,s,\gamma))}(z))$ at the corresponding origin of scattering potential type α, which is found at cavity site $\vec{R}_I + \vec{b}_s$ when this is filled according to configuration γ:

$$[\underline{\underline{F}}^{(\gamma,\gamma')}(z)]_{I,s,L;J,s',L'} = Z_L^{(\alpha(I,s,\gamma))}(z)Z_{L'}^{(\alpha(J,s',\gamma'))}(z),$$
$$[\underline{\underline{F}}^{(\gamma)}(z)]_{I,s,L;J,s',L'} = Z_L^{(\alpha(I,s,\gamma))}(z)Z_{L'}^{(\alpha(J,s',\gamma))}(z),$$

and:

$$[\underline{\underline{\underline{\underline{ZJ}}}}^{(\gamma)}(z)]_{I,s,L;J,s',L'} = \delta_{I,J}\delta_{s,s'}\delta_{L,L'} \cdot Z_L^{(\alpha(I,s,\gamma))}(z)J_{L'}^{(\alpha(J,s',\gamma))}(z)\,.$$

We refer to Ref. [19] for the original introduction of all these quantities in their single-site form.

With this, the three terms of Eq. (4) read, respectively:

$$\underline{\underline{\overline{G}}}^{(\rm CD)}(z) = \sum_{\gamma=1}^{N_{\rm tot}} P(\gamma)(\underline{\underline{F}}^{(\gamma)}(z)\odot\underline{\underline{D}}^{(\gamma)}(z)\underline{\underline{\overline{t}}}(z) - \underline{\underline{\underline{\underline{ZJ}}}}^{(\gamma)}(z)), \tag{6}$$

which is the effective medium Green function, associated with $\vec{R}_I + \vec{b}_s$, $\vec{R}_J + \vec{b}_{s'}$ within the same cavity, i.e., "cavity diagonal" (and sufficient as remarked above to compute the DOS as: $\overline{n}(z) = -\frac{1}{\pi}\Im(Tr(\underline{\underline{\overline{G}}}^{(\rm CD)}(z)))$ for instance);

$$\underline{\underline{\overline{G}}}^{(\rm NCD)}(z) = \sum_{\gamma,\gamma'=1}^{N_{\rm tot}} P(\gamma)P(\gamma')\underline{\underline{F}}^{(\gamma,\gamma')}(z) \odot \underline{\underline{D}}^{(\gamma)}(z)\underline{\underline{\overline{t}}}(z)\underline{\underline{\tilde{D}}}^{(\gamma')}(z), \tag{7}$$

[where $\underline{\underline{\tilde{D}}}^{(\gamma')}(z) = (\underline{\underline{D}}^{(\gamma')}(z))^T$] which is a dispersion-less second term, which cancels back the first one in a LRO regime where the impurity projectors reduce to identities and $\underline{\underline{F}}^{(\gamma,\gamma')}(z)$ simply corresponds to $\underline{\underline{F}}^{(\gamma)}(z)$, and finally:

$$\underline{\underline{\overline{G}}}^{(\rm NCD)}(\vec{k},z) = \sum_{\gamma,\gamma'=1}^{N_{\rm tot}} P(\gamma)P(\gamma')\underline{\underline{F}}^{(\gamma,\gamma')}(z) \odot \underline{\underline{D}}^{(\gamma)}(z)\underline{\underline{\overline{t}}}^{(\vec{K}_n(\vec{k}))}(\vec{k},z)\underline{\underline{\tilde{D}}}^{(\gamma')}(z) \tag{8}$$

for the last term, which is the only one to remain in the LRO limit but cancels out the second one of Eq. (7) upon integrating over $\vec{k}\in\mathbf{\Omega}_{\rm BZ}$, thus showing the possible reduced evaluation of Eq. (4) simply to Eq. (6) in particular cases.

A. Tile boundary discontinuities

The crucial point in our discussion is that, contrary to the original single-site-only theory, the NLCPA-extended effective medium scattering path operator matrix, $[\underline{\underline{\overline{\tau}}}^{(\vec{K}_n(\vec{k}))}(\vec{k},z)]_{I,J} = \underline{\underline{\overline{\tau}}}^{(\vec{K}_n(\vec{k}))}(\vec{k},z)e^{+i\vec{K}_n\cdot(\vec{R}_I-\vec{R}_J)}$ is presently constructed from a different argument and will be in general discontinuously different, depending on the coarse-graining tile $\mathbf{\Omega}_{\rm BZ}(\vec{K}_n)$ where the desired $\vec{k}\in\mathbf{\Omega}_{\rm BZ}$ lies. The theory in fact prescribes, taking also into account its further multisublattice generalization [22,26]:

$$\underline{\underline{\overline{\tau}}}^{(\vec{K}_n(\vec{k}))}(\vec{k},z) = (\underline{\underline{\overline{m}}}(\vec{K}_n,z) - \underline{\underline{\tilde{g}}}(\vec{k},z))^{-1}, \tag{9}$$

where $\underline{\underline{\tilde{g}}}(\vec{k},z)$ is the structure constant matrix, inclusive of the intersublattice correction of Ref. [26], and $\underline{\underline{\overline{m}}}(\vec{K}_n,z)$ contains SRO-dependent local environment effects, up to a resolution inversely proportional to the cavity size $N_c\times N_{\rm sub}$.

This coarse-graining tiling is however only defined by the requirement of preserving all point group symmetries of the direct space lattice, upon splitting the Brillouin zone into equal volume, nonoverlapping regions such that [9]:

$$\begin{aligned}\mathbf{\Omega}_{\rm BZ} &= \mathbf{\Omega}_{\rm BZ}^{(\rm cav)}(\vec{K}_1)\bigcup\ldots\bigcup\mathbf{\Omega}_{\rm BZ}^{(\rm cav)}(\vec{K}_{N_c}),\\ \emptyset &= \mathbf{\Omega}_{\rm BZ}^{(\rm cav)}(\vec{K}_I)\bigcap\mathbf{\Omega}_{\rm BZ}^{(\rm cav)}(\vec{K}_J)\quad\forall\, I\neq J,\end{aligned} \tag{10}$$

together with the requirement that the "cluster momenta" $\vec{K}_n$ labeling these should be conserved [8]. This corresponds to an idempotency condition:

$$\frac{1}{N_c}\sum_{n=1}^{N_c} e^{+i\vec{K}_n\cdot(\vec{R}_I-\vec{R}_J)} = \delta_{IJ}, \tag{11}$$

which as noted in Refs. [24,37] remains valid up to a rigid shift of each $\vec{K}_n$ by a "tiling phase" $\vec{\phi} = (\phi_x,\phi_y,\phi_z)\in\mathbf{\Omega}_{\rm BZ}$. By placing however the tiles boundaries at different locations within the Brillouin zone, the discontinuous jump in $\vec{k}$-dependent, NSD quantities such as the BSF will also be translated and acquire in general different magnitudes.

Furthermore, NLCPA coarse-grained integrations will also collect results differently as a function of $\vec{\phi}$. This leads to a different ability of the effective medium to pick up local environment effects. On one extreme we may have for instance the choice which, for a $N_c = 2$ simplest example, coarse grains within individual tiles all points closest to $\vec{\Gamma}$/furthest from it (as illustrated in Fig. 2(a), left panel). In another limit and for the same cavity size and occupation statistics, there can be a choice leading to combining contributions from alternating octants of $\vec{\Gamma} = (0,0,0)$, regardless of distances (Fig. 2(e), left panel). Practical consequences in the two cases are illustrated through a concrete example in Sec. III A. As one can anticipate from the above simple geometrical argument, in one case we have strongest sensitivity to a SRO statistics that enforces having alike/unalike nearest neighbors within the cavity. In the other one, the NLCPA will not be able to discriminate at all the different scenarios and collapses once again to the same results as those of the single-site CPA.

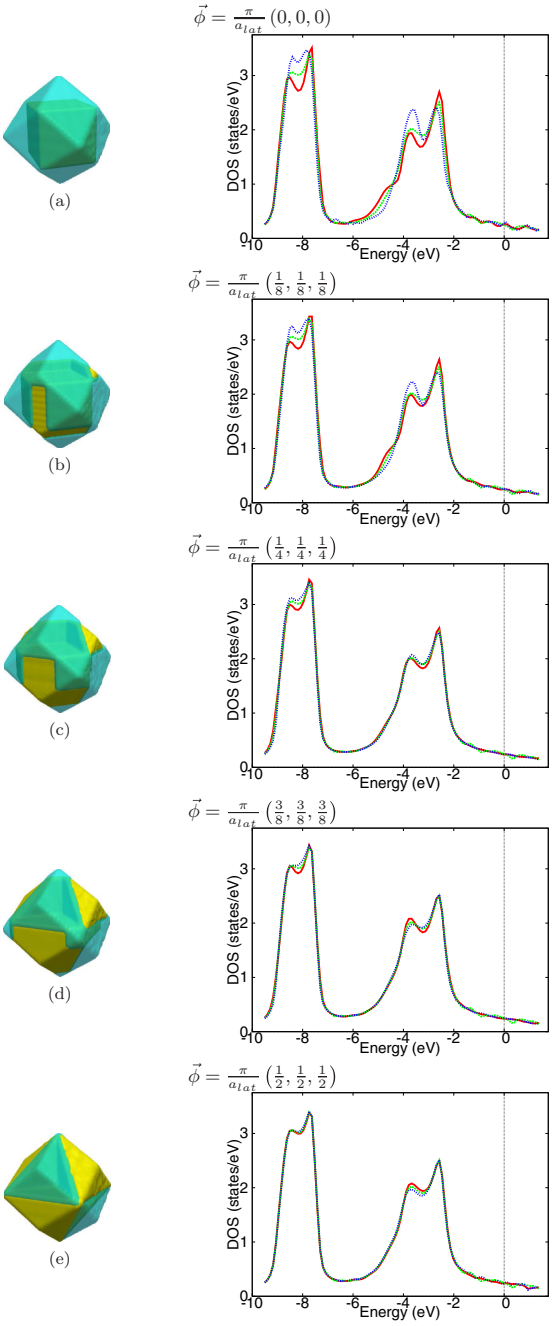

FIG. 2. $N_c = 2$ NLCPA Brillouin zone coarse-graining (left) and corresponding DOS (right) of *bcc* $Cu_{50\%}$,$Zn_{50\%}$ for the three scenarios of Table I: $SRO = -1$ (blue)/0 (green)/+1 (red), as a function of tiling phase choice (top to bottom).

B. Remedial strategy: $N_c > 1$, $N_{\text{sub}} = 1$ scenario

A practical solution to address both such aspects of the coarse graining has been [24,37] to sample the tiling phase dependence through the choice of $N_p > 1$ tiling phases $\vec{\phi}$'s and average over individual results according to:

$$\overline{\overline{G}}(\vec{k},z) := \frac{1}{N_p}\sum_{\vec{\phi}}^{N_p} \overline{G}^{(\vec{\phi})}(\vec{k},z). \tag{12}$$

As shown in Sec. III A for a first benchmark application to the KKR study of real materials, this procedure successfully removes the spurious tiling phase freedom, already upon using a very small N_p. We can also appreciate how, despite there being a lowered sensitivity to SRO, the prescription does not correspond to canceling out all local environment influences that the NLCPA was designed to describe.

It should finally be remarked that although purely SD observables, such as the DOS, can be defined in terms of Eq. 6 alone, and appear at first glance exempt from tiling artifacts even without the additional sampling of Eq. (12), such an extra step should in general always be undertaken in order to remove dependence of results on any arbitrarily chosen single $\vec{\phi}$ (Fig. 2, right panels). This can be appreciated as an obvious consequence of the heavy dependence of the BSF from the full formula of Eq. (4) on $\vec{\phi}$ and the DOS being its $\vec{k} \in \mathbf{\Omega}_{\text{BZ}}$ integral.

Benchmark results for the full expression are given in Fig. 4 and further discussed in the following, considering for better clarity as a second example the case of single energy point slices for the effective medium spin resolved $\overline{A}^{(\sigma)}(\vec{k},E)$ (single tiling phase results for $\vec{\phi} = (0,0,0)$ following the notation of Eq. (12)) and $\overline{\overline{A}}^{(\sigma)}(\vec{k},E)$ ($N_p > 1$-averaged results) of a fcc $Fe_{75\%},Pd_{25\%}$ test case.

C. Remedial strategy: $N_c = 1$, $N_{\text{sub}} > 1$ scenario

To complete discussion of the tiling phase freedom consequences on the NLCPA effective medium, it remains to consider the complementary scenario where all SRO structure comes through $P(\gamma)$'s defined over a $N_c = 1$ but $N_{\text{sub}} > 1$-wide cavity. The situation may be to first examination less obviously in need of amendments, because we are now dealing with a tile as big as the whole Brillouin zone. We never cross therefore a boundary in evaluating for instance the BSF along a path between representative high-symmetry points. It can be argued however that an extra step in the form of Eq. (12) is still needed for full theoretical consistency. Formally in fact we are still relying on both direct space truncation to a finite cavity size and Fourier transformations within the now $(L_{\max} \times N_{\text{sub}}) \times (L_{\max} \times N_{\text{sub}})$ CPA scattering path operator. Both such factors still limit the effective medium's ability to pick up SRO effects beyond a certain direct space radius and associate them unequivocally to a certain $\vec{k} \in \mathbf{\Omega}_{\text{BZ}}$. From a more applied point of view, the same conclusion can also be drawn as recalled before by comparing two different ways to describe the same physical system and demanding in either case the formalism to produce identical observables as remarked in the introduction.

As shown in Refs. [25,26], it is a careful handling of the intersublattice scattering path operator blocks that enriches the multisublattice CPA of Pindor *et al.* [34] with sensitivity to SRO, in complete agreement with the single sublattice NLCPA. Considering at first the DOS and the representative, simplest benchmark test cases of a $N_c = 2$, $N_{\text{sub}} = 1$ *bcc* binary alloy versus its fully analogous $N_c = 1$, $N_{\text{sub}} = 2$ CsCl-like unit cell or a $N_c = 4$, $N_{\text{sub}} = 1$ fcc lattice visualized in terms of a $N_c = 1$, $N_{\text{sub}} = 4$ Cu_3Au-like unit cell, the above "multisublattice" NLCPA prescription could be demonstrated

to lead in fact to the same SD results, with the "default" choice $\vec{\phi} = (0,0,0)$, and reliance on the shortened expression of Eq. (6).

This is however no longer the case for the BSF from the full Eq. (4), particularly as $\vec{\phi}$ is changed. As discussed, the $N_c > 1$, $N_{\rm sub} = 1$ problem representation will exhibit moving discontinuities, while the $N_c = 1$, $N_{\rm sub} > 1$ case appears at first sight artifact free, owing simply to there not being the necessity to evaluate quantities which involve crossing the boundary of the single tile, now as big as the Brillouin zone. This conundrum can however be tackled by recalling that in the second case we are still considering in reality two roles for $\mathbf{\Omega}_{\rm BZ}$ that no longer automatically coincide as in the original single-site theory. In the first one, it is the domain of evaluation points $\vec{k}$ for the BSF which occur in particular as the argument of Eq. (8) and specifically in the structure constants term of Eq. (9). In the second one, $\mathbf{\Omega}_{\rm BZ}$ is the single tile within which the (NL)CPA effective medium is approximated as energy dependent but $\vec{k}$ constant. For this purpose $\vec{k}$ acts through self-consistent determination of an appropriate value $\underline{\underline{\tau}}(\vec{K}_1,z)$, such that:

$$\underline{\underline{\tau}}(\vec{k},z) \simeq \underline{\underline{\tau}}(\vec{K}_1,z) \qquad \forall \vec{k} \in \mathbf{\Omega}_{\rm BZ}^{\rm (cav)}(\vec{K}_1), \tag{13}$$

and in the multisublattice extension of the theory it is in the sublattice off-diagonal blocks of the scattering path operator where the SRO sensitivity is built up. As discussed in Ref. [26], this is associated with the intersublattice structure constants correction: $[\underline{\underline{\tilde{g}}}(\vec{k},z)]_{s,s'} = [\underline{\underline{g}}(\vec{k},z)]_{s,s'} e^{-i\vec{k}\cdot(\vec{b}_s - \vec{b}_{s'})}$. To recover full agreement with the $N_c > 1$, $N_{\rm sub} = 1$ results of the same physical system as a function of the tiling phase freedom, it is hence sufficient to explicitly consider the argument $\vec{k}$ in this expression as relative to the origin of the (single) tile $\mathbf{\Omega}_{\rm BZ}^{\rm (cav)}(\vec{K}_1)$, which can be in general subject to $\vec{\phi}$ shifts also in these $N_c = 1$, $N_{\rm sub} > 1$ scenarios. By replacing $\vec{k}$ with $\vec{k} + \vec{\phi}$, again the proposal of Eq. (12) can be applied, leading to the same renormalized results for SD as well as NSD observables upon taking the average over $N_p > 1$ tiling phases. We illustrate the point by referring again for full clarity to the same $Cu_{50\%}$,$Zn_{50\%}$ binary alloy and one representative SRO regime in Fig. 2, now evaluating the BSF as a function of $\vec{\phi}$ within a CsCl-like cavity construction (Fig. 3).

III. RESULTS

A. Comparison with previous results: The example of $Cu_{50\%}$,$Zn_{50\%}$

We devote the first part of this section to a rapid review of the familiar $Cu_{50\%}Zn_{50\%}$ *bcc* $a_{\rm lat} = 2.87$ [Å] alloy example, in light of the tiling phase average proposal above. Figure 2 depicts the effective medium DOS $\overline{n}(E)$ from Eq. (6) for $N_c = 2$ and as a function of NLCPA tiling phase $\vec{\phi}$. In all cases the same three extremal SRO regimes associated with the Warren-Cowley parameter [38,39] values -1,0 or $+1$ (Table I) have been examined.

As remarked, previous KKR-NLCPA calculations [10,13,26] on this benchmark system have been initially carried out only with the implicit choice $\vec{\phi} = \frac{\pi}{a_{\rm lat}}(0,0,0)$ that corresponds to the results of the upper panel of Fig. 2(a). This partitioning of reciprocal space leads to the strongest

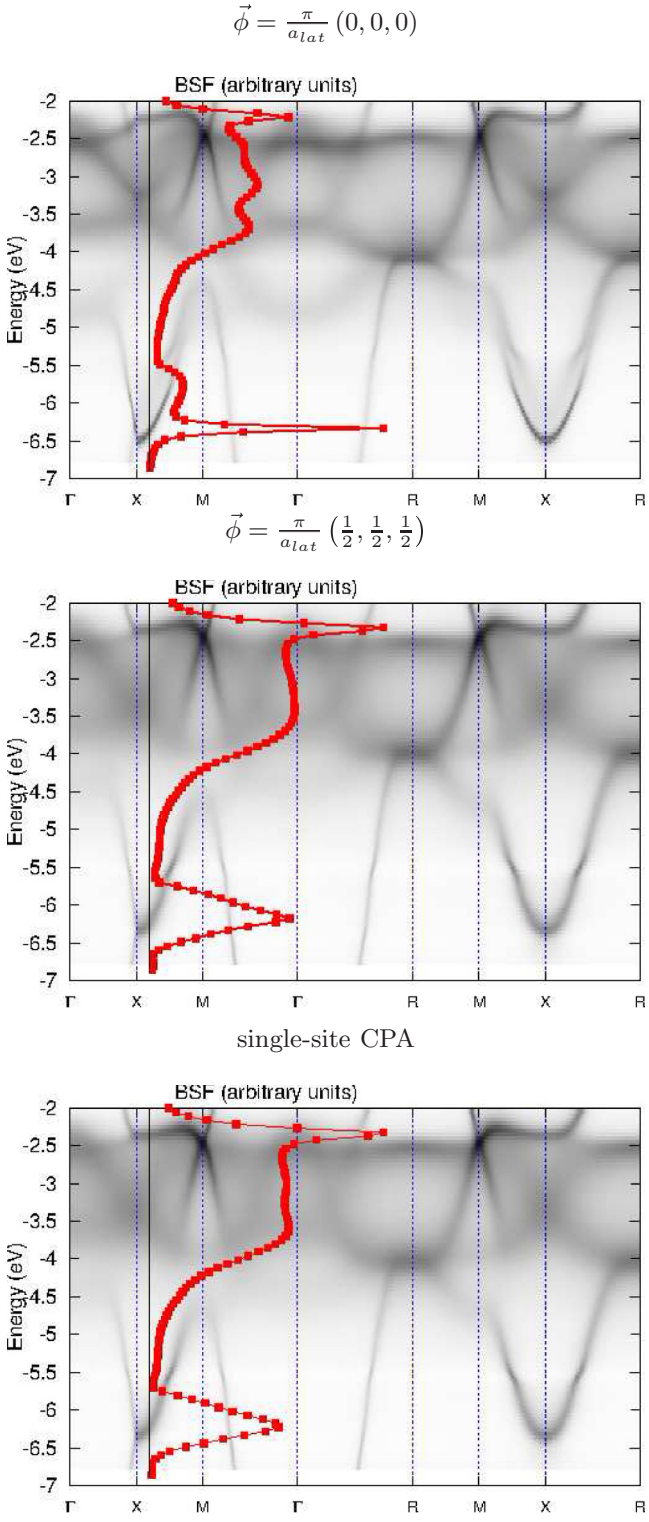

FIG. 3. $N_c = 1$ Multisublattice (MS)NLCPA BSF of *bcc* $Cu_{50\%}$,$Zn_{50\%}$ evaluated as a $N_c = 1$, $N_{\rm sub} = 2$ CsCl unit cell and the $SRO = +1$ regime from Table I. Maximal local environment effects are picked up for $\vec{\phi} = (0,0,0)$ (top) and disregarded for $\vec{\phi} = \frac{\pi}{a_{\rm lat}}(\frac{1}{2},\frac{1}{2},\frac{1}{2})$ (middle); thus falling back onto the same predictions as from the single-site CPA (bottom). The intensity of the underlying BSF as a function of energy, along a fixed arbitrarily chosen point $\vec{k} = (0.5,0.158,0.)$ (black line) is also highlighted (red overlay), exhibiting peaks with full-width-at-half-maximum (FWHM) inversely proportional to the lifetime of the intercepted bands [23].

TABLE I. Warren-Cowley SRO parameter [39], explicit listing of cavity configurations γ's and associated probability distributions $P(\gamma)$ for a $N_c \times N_{\rm sub} = 2 \times 1$ sites NLCPA model of a $Cu_{50\%}$,$Zn_{50\%}$ alloy in the *bcc* phase. Single-site CPA calculations correspond to a $SRO = 0$, fully uncorrelated scenario, here reproduced by explicitly considering all the $N_{\rm tot} = 2^2 = 4$ possible configurations γ for this cavity size. The DOS associated with each case is given as a function of $\vec{\phi}$ in Fig. 2.

Local order regime	Cavity configurations	Probability
$SRO = -1$	$\gamma_1 = \{Cu,Zn\}$	$P(\gamma_1) = 50\%$
	$\gamma_2 = \{Zn,Cu\}$	$P(\gamma_2) = 50\%$
$SRO = 0$	$\gamma_1 = \{Cu,Cu\}$	$P(\gamma_1) = 25\%$
	$\gamma_2 = \{Cu,Zn\}$	$P(\gamma_2) = 25\%$
	$\gamma_3 = \{Zn,Cu\}$	$P(\gamma_3) = 25\%$
	$\gamma_4 = \{Zn,Zn\}$	$P(\gamma_4) = 25\%$
$SRO = +1$	$\gamma_1 = \{Cu,Cu\}$	$P(\gamma_1) = 50\%$
	$\gamma_2 = \{Zn,Zn\}$	$P(\gamma_2) = 50\%$

resolution of SRO effects, that are associated with correlation in the arrangement of nearest neighbors impurities in direct space. In this case in fact the Brillouin zone tiling of Eq. (10) distinguishes between an inner cubic region $\mathbf{\Omega}_{\rm BZ}^{\rm (cav)}(\vec{K}_1)$ around $\vec{\Gamma}$ (Fig. 2 left column, in yellow) and a peripheral one $\mathbf{\Omega}_{\rm BZ}^{\rm (cav)}(\vec{K}_2)$ (Fig. 2 left column, in blue) which can also be interpreted as an equivalent cubic domain, just shifted along one axis and folded back at the periodic boundary of $\mathbf{\Omega}_{\rm BZ}$. On the negative side, evaluation of the BSF according to Eq. (4) clearly reveals the discontinuities problem upon crossing such a boundary (Fig. 1), as also noted in Ref. [22].

As we progressively vary the tiling phase towards $\vec{\phi} = \frac{\pi}{a_{\rm lat}}(\frac{1}{2},\frac{1}{2},\frac{1}{2})$, the situation morphs into a scenario where reciprocal space points are no longer coarse grained around cluster momenta $\vec{K}_n$ that lie all closer or farther away from $\vec{\Gamma}$. Correspondingly, the difference in DOS results between various SRO regimes is gradually lost (Figs. 2(a)–2(e)), thus reproducing in this 3D SCF-DFT [40] KKR examination of a *bcc* metallic alloy the same conclusions of 1D *sc* (simple cubic) tight-binding model calculations reported in Fig. 4 of Ref. [24].

The same dependence can be observed also in a $N_c = 1$, $N_{\rm sub} = 2$ treatment of the same system, carried out according to the extended theory of Sec. II C for the full expression of the BSF Eq. (4) (Fig. 3). In this case the theory produces for each choice of $\vec{\phi}$ a smooth band structure, in which specific features associated with local environment effects can be discerned but remain sensitive to any single choice of tiling phase, until falling back on the single-site CPA results.

Upon taking the tiling phase average of Eq. (12) across the parameter sampling space, the final result displays therefore reduced influence of SRO for any fixed cavity size $N_c \times N_{\rm sub}$. The outcome remains however distinct from the fully uncorrelated scenario that the single-site CPA implicitly enforces. We come to this point in better detail through the next example of Sec. III B.

B. A simple unit cell, substitutional disorder example: $Fe_{75\%}$,$Pd_{25\%}$

We consider here for further illustration purposes the test case of an iron-palladium alloy in the stoichiometric ratio

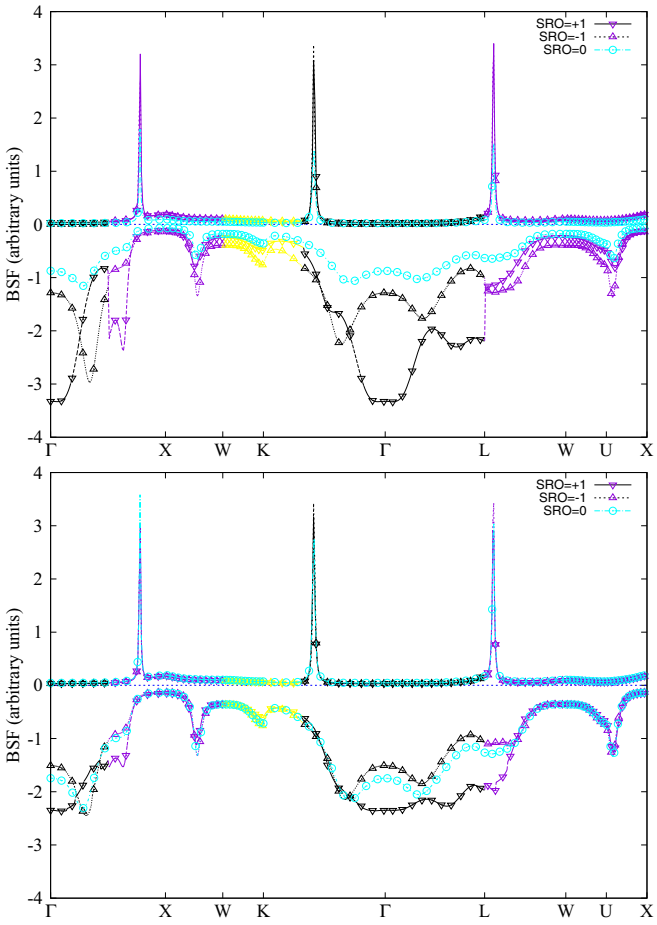

FIG. 4. Fixed energy slice of the BSF for $Fe_{75\%}Pd_{25\%}$ at $E \simeq E_F$. Each $\vec{k}$ point is color-coded depending on the particular $\mathbf{\Omega}_{\rm BZ}^{\rm (cav.)}(\vec{K}_n)$ NLCPA tile it belongs to, for a $N_c = 4$ $N_{\rm sub} = 1$ partitioning with $\vec{\phi} = (0,0,0)$. Different symbols denote results pertaining to different SRO regimes; positive (negative) sign is used to resolve majority (minority) spin channels. Calculations performed with a single tiling phase choice (top) show unphysical, SRO-dependent discontinuities upon crossing tile boundaries, such as at the $\vec{L}$ point. The extra tiling phase averaging step of Eq. (12) removes such artifacts, while retaining appreciable sensitivity to SRO effects (bottom).

3 : 1. The phase diagram of this material shows, for suitable preparation procedures [41], a $N_{\rm sub} = 1$ *fcc* geometry and has been experimentally investigated as a function of SRO by comparing samples either suddenly quenched or slowly cooled from the melting temperature [42].

In our discussion such a system is presently taken just as a simple prototype of a substitutionally disordered real material, on which to deploy the developments of Sec. II B as a function of cavity size, and in combination with spin-dependent effects. We consider in particular for fixed lattice parameter $a_{\rm lat} = 3.78$ [Å] two opposite SRO regimes, both reproducing the same overall concentration $c_{\rm Fe} = 75\%$, and corresponding for ease of comparisons to the extremal scenarios of Table I.

In the first case, full local clustering ($SRO = +1$) simulates again the situation where alike atomic species would tend to appear on average next to each other. In the second, full local ordering case ($SRO = -1$), the two different

TABLE II. Warren-Cowley SRO parameters [39], explicit listing of cavity configurations γ's, and associated probability distributions $P(\gamma)$ for a $N_c \times N_{\rm sub} = 4 \times 1$ sites NLCPA model of a $Fe_{75\%}$,$Pd_{25\%}$ alloy in the fcc phase. Single-site CPA results correspond to a $SRO = 0$, fully uncorrelated scenario, given by all the $N_{\rm tot} = 2^4 = 16$ configurations γ of this cavity size, each with factorized probability: $P(\gamma) = \prod_{I=1}^{N_c} \prod_{s=1}^{N_{\rm sub}} c_{\alpha(I,s,\gamma)}$ with $\alpha(I,s,\gamma) =$ Fe or Pd.

Local order regime	Cavity configurations	Probability
$SRO = -1$	$\gamma_1 =$ {Fe,Fe,Fe,Pd}	$P(\gamma_1) = 25\%$
	$\gamma_2 =$ {Fe,Fe,Pd,Fe}	$P(\gamma_2) = 25\%$
	$\gamma_3 =$ {Fe,Pd,Fe,Fe}	$P(\gamma_3) = 25\%$
	$\gamma_4 =$ {Pd,Fe,Fe,Fe}	$P(\gamma_4) = 25\%$
$SRO = +1$	$\gamma_1 =$ {Fe,Fe,Fe,Fe}	$P(\gamma_1) = 75\%$
	$\gamma_2 =$ {Pd,Pd,Pd,Pd}	$P(\gamma_2) = 25\%$

species tend instead to intermix as much as possible. Both scenarios are here presented on the same footing, even if only the latter phase would be thermodynamically favored [43]. Their statistics are summarized for a NLCPA cavity of $N_c \times N_{\rm sub} = 4 \times 1$ sites in Table II. Conversely, the $SRO = 0$ situation which is always implicitly enforced by the single-site CPA corresponds to a complete lack of nearest neighbor correlation between Fe or Pd atoms. It can be set up in this description by considering all the $N_{\rm tot} = 2^4 = 16$ possible configurations $\gamma_1 =$ {Fe,Fe,Fe,Fe}, $\gamma_2 =$ {Fe,Fe,Fe,Pd}, $\gamma_3 =$ {Fe,Fe,Pd,Pd}, ..., $\gamma_{15} =$ {Pd,Pd,Pd,Fe}, $\gamma_{16} =$ {Pd,Pd,Pd,Pd}, each with a purely factorized probability distribution $P(\gamma) = \prod_{I=1}^{N_c} \prod_{s=1}^{N_{\rm sub}} c_{\alpha(I,s,\gamma)}$ for $\alpha(I,s,\gamma) =$ Fe or Pd. In all cases, disorder affects most significantly the minority spin channel, consistent with previous investigations of other ferromagnetic transition metals alloys [44,45].

We apply here the full expression of Eq. (4) and show in particular for better clarity $\vec{k}$-resolved BSF slices at a single energy point close to the Fermi level. With the single choice $\vec{\phi} = \frac{\pi}{a_{\rm lat}}(0,0,0)$, i.e., the Brillouin zone coarse graining depicted in Fig. 5, one can clearly observe how the NLCPA

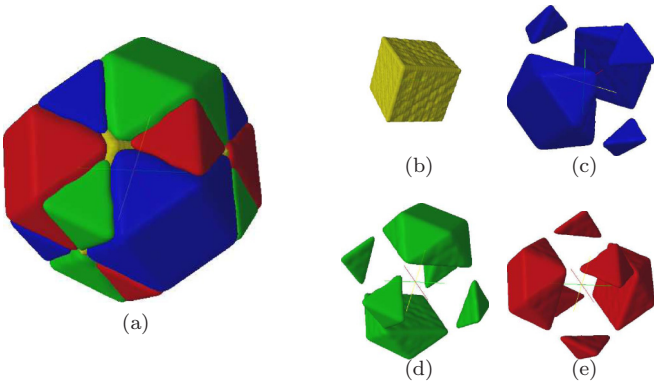

FIG. 5. NLCPA $N_c = 4$ tiling for a fcc geometry (panel a: entire Brillouin zone $\mathbf{\Omega}_{\rm BZ}$, color-coded), matching the construction of Table I from Ref. [8] and corresponding to a tiling phase choice: $\vec{\phi} = \frac{\pi}{a_{\rm lat}}(0,0,0)$ which identifies a central cubic tile around $\vec{\Gamma}$ (panel b) and three equivalent volume regions along the k_x,k_y, and k_z axes (panels c–e: expanded view).

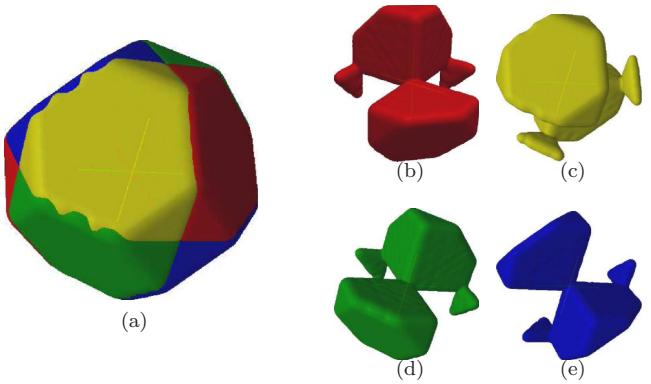

FIG. 6. NLCPA $N_c = 4$ tiling for a fcc geometry (panel a: entire Brillouin zone $\mathbf{\Omega}_{\rm BZ}$, color-coded), matching the construction of Table I from Ref. [8] and corresponding to a tiling phase choice: $\vec{\phi} = \frac{\pi}{a_{\rm lat}}(-\frac{1}{2}, -\frac{1}{2}, -\frac{1}{2})$ which identifies four equivalent tiles around $\vec{\Gamma}$, each along different axial diagonals (panels b–e: expanded view).

results show an unphysical jump in combination with either extreme forms of SRO (but not in the 'special' case of fully uncorrelated impurities, for which the extended formalism does not differ from the one implicitly assumed by the single-site CPA), and only in the spin channel which has been actually affected by loss of LRO (Fig. 4, top). The artifact is furthermore located in correspondence with crossing the boundary between the inner tile $\mathbf{\Omega}_{\rm BZ}^{\rm (cav)}(\vec{K}_1 = \vec{\Gamma})$ and any of the outer ones $\mathbf{\Omega}_{\rm BZ}^{\rm (cav)}(\vec{K}_2)$, $\mathbf{\Omega}_{\rm BZ}^{\rm (cav)}(\vec{K}_3)$, $\mathbf{\Omega}_{\rm BZ}^{\rm (cav)}(\vec{K}_4)$. We observe instead continuity in results across these, as expected due to their equivalence from the point of view of the particular SRO regimes being set up (Table II).

Upon averaging over a few tiling phase choices between $\vec{\phi} = (0,0,0)$ (Fig. 5) and $\vec{\phi} = \frac{\pi}{a_{\rm lat}}(\frac{1}{2}, \frac{1}{2}, \frac{1}{2})$ (Fig. 6) according to Eq. (12), all artifacts are successfully removed (Fig. 4 (bottom). Although the difference between different disordered scenarios is reduced, results remain sensitive to the adopted statistics, in line with our expectations from Sec. II and consistently with the insight already gained from the DOS of Eq. (6), as depicted in Fig. 2.

We finally consider for the relevant spin channel of this test case calculation the particular influence of the number of unit cells in the cavity, N_c, as a further parameter defining how far complete local clustering, i.e., SRO $= +1$ is on average enforced. This is shown in Fig. 7 for the cases $N_c = 1$ (which corresponds to the original single-site theory), $N_c = 4$, and $N_c = 32$. As it could be easily anticipated, the effective medium BSF acquires now progressively a sharper outlook, which is a consequence of longer mean free path for electrons that are meeting larger and larger portions of homogeneous Fe or Pd atoms. The positions of the corresponding Lorentzian peaks can be in particular compared with the limit LRO scenarios of an either 100% Fe or 100% Pd sample (Fig. 8, top and bottom).

C. A complex unit cell, disordered local moment example

On the complex unit cell side, after the technical illustration of Fig. 3, we come to the less artificial example of the normal state of the iron-based superconductor FeSe. The

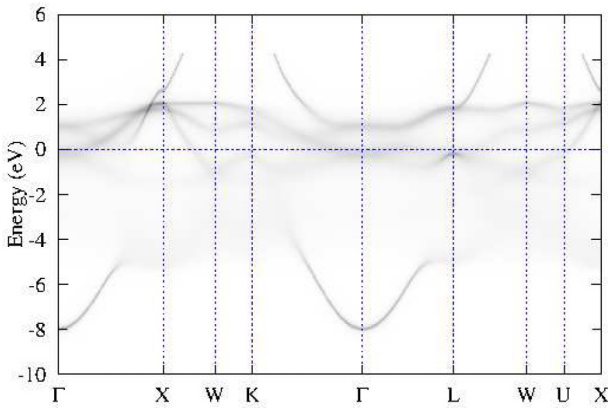

(a) $SRO = 0$ $N_c = 1$

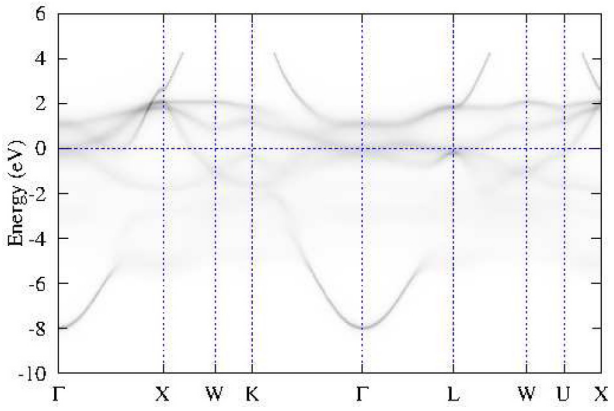

(b) $SRO = +1$ $N_c = 4$

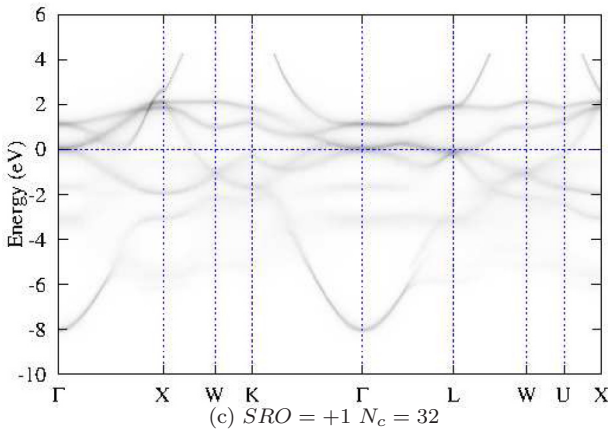

(c) $SRO = +1$ $N_c = 32$

FIG. 7. Minority spin BSF of $Fe_{75\%}Pd_{25\%}$ as a function of the NLCPA cavity size (top: $N_c = 1$; center: $N_c = 4$; bottom: $N_c = 32$), for the same $SRO = +1$ model of complete local clustering of alike atomic species. The tiling phase averaging of Eq. (12) has led to artifact-free results across the entire Brillouin zone. As the size of the NLCPA cavity increases, sharper features emerge from the heavily smeared out single-site CPA calculation and tend to progressively reproduce the same outlook which would be given by a concentration-weighted sum of the individual BSF's of either LRO Fe or Pd (Fig. 8).

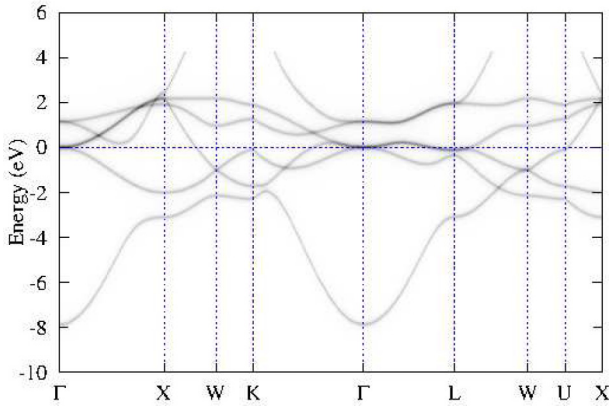

(a) *LRO Fe*

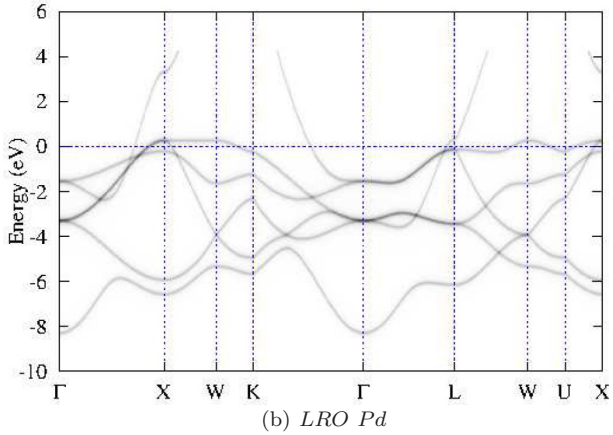

(b) *LRO Pd*

FIG. 8. Minority spin BSF of either pure Fe (top) or pure Pd (bottom) in a LRO arrangement, within the same fcc lattice as the $Fe_{75\%}$,$Pd_{25\%}$ alloy of Fig. 7.

phase diagram of this material is characterized by lack of magnetic LRO down to low temperature, together with experimental [46,47] and theoretical [48] evidence that locally Fe moments should align in a nearest neighbors striped order. This scenario can be simulated with the formalism of Sec. II by means of a $N_c = 1$, $N_{\text{sub}} = 8$ cavity, corresponding to the rotated and doubled primitive unit cell and with disorder confined to the magnetic degree of freedom of the four iron sites thus exposed in a square array. We examine in Fig. 9 the corresponding tiling phase-averaged BSF for the tetragonal lattice phase, as a function of increasing competition between the particular configuration γ which alone would describe LRO stripes, and all other local patterns which can in principle be realized within this cavity size. The collapse of the lifetime of Bloch's states is very rapid, with individual band features quickly disappearing in a rather undistinguished, fully blurred outlook, that matches single-site CPA-DLM results for $P(\gamma_1) = P(\gamma_2) = \ldots = P(\gamma_{16}) = 6.25\%$. Our extended method gives however also access to the full electronic structure of the material in intermediate scenarios. Further comparisons with experiments, together with usage of the corresponding effective medium construction for evaluation of additional observables beside the BSF alone, can lead to more specific predictions concerning the actual extent of nematicity within such a model and its relevance for the peculiar physics of this compound.

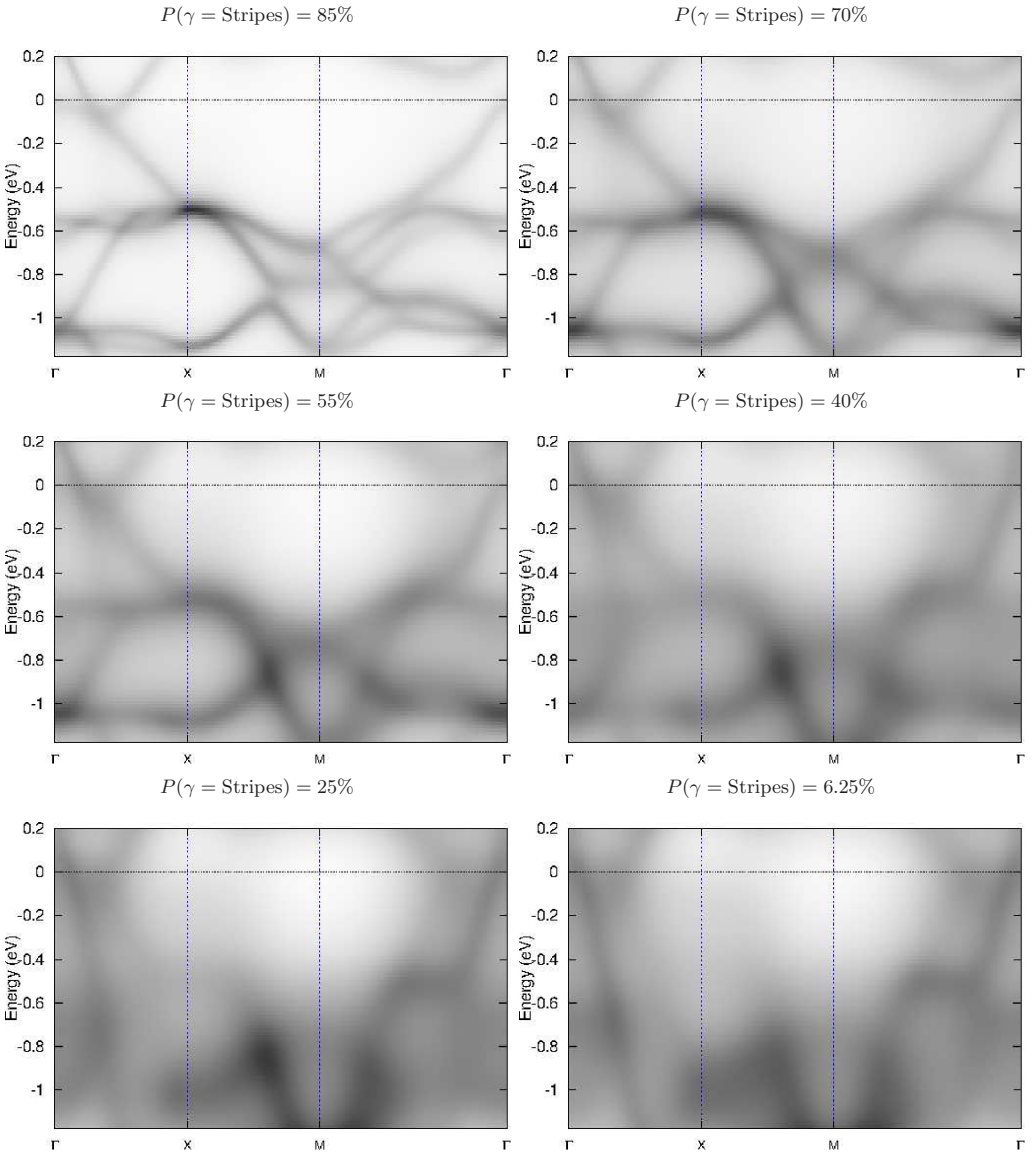

FIG. 9. DLM BSF of FeSe from a $N_c = 1$ $N_{\text{sub}} = 8$-wide NLCPA cavity, with magnetic disorder only on the four Fe sublattices. The probability of a specific striped pattern in the iron moments is progressively reduced, down to equal likelihood across all the $N_{\text{tot}} = 4^2 = 16$ cavity configurations. Intermediate regimes allow us to simulate this compound's lack of magnetic LRO down to low temperature, together with partial, local persistence of particular forms of SRO.

IV. CONCLUSIONS

We have reviewed the NLCPA for the first principles study of various kind of SRO and disorder effects in real materials. The formalism has been in particular re-examined from the point of view of NSD observables such as the Bloch spectral function. After discussing the physical origin of unwanted artifacts in $\vec{k}$-resolved quantities, a scheme for their removal through multiple sampling of a tiling phase freedom intrinsic to the NLCPA/DCA techniques has been applied at the KKR-SCF-DFT level for various systems. Its discussion has been furthermore extended to cover the case of complex unit cell materials. We also examine its implications for SD observables such as the density of states which have historically been among the first applications of the theory in its original form.

The generalized framework has been assessed by revisiting well established case studies as well as original examples. The aspects of practical implications from any given tiling phase choice, NLCPA cavity size, and probabilistic dominance of a given random pattern with respect to all others have been systematically illustrated, through application to substitutional disorder in metallic alloys as well as paramagnetism in the prototypical iron-based superconductor FeSe.

ACKNOWLEDGMENTS

Brief hospitality at the Physics Department of the University of Milan during part of this work is gratefully acknowledged, as well as a longer stay at the National Institute of Advanced Industrial Science and Technology (AIST), Tsukuba. A.M. gratefully acknowledges discussion

with Prof. Peter Entel at University of Duisburg-Essen, which in part motivated the present developments, together with very enjoyable brief exchanges with Prof. Antonios Gonis and Prof. G. Malcolm Stocks. Possible application to FeSe developed from insightful discussion with Prof. Igor Mazin.

APPENDIX A: IMPACT ON COMPUTATIONAL REQUIREMENTS

In the original CPA the effective medium is computed by solving $\sum_{s=1}^{N_{\rm sub}} N_{alt}(s)$ 'impurity problems' for the single-site transition matrix $\underline{t}^{(\alpha(s))}(z)$ in L,L' and associated scattering path operator $\underline{\tau}^{(\alpha(s))}(z)$, where $\alpha(s)$ labels the scattering potential found on sublattice s. Computational requirements thus grow only linearly when moving from binary to ternary or more complex scenarios, such as in the topical example of high-entropy alloys [49–53].

The method also involves repeated reciprocal space integrations over the Brillouin zone, with a computational cost only dependent on $\vec{k}$ sampling resolution. In the DCA/NLCPA extension of the technique this operation is performed in a coarse-grained fashion, simply collecting distinct results across the N_c tiles. The generalized algorithm adds an extra step of coupled lattice Fourier transformations, whose cost grow with N_c. This can be optimized by resorting to fast Fourier transformations (FFT) although practically such need has not been met yet, due to relatively small cavity sizes so far considered in KKR applications. Since N_c represents also the NLCPA cavity size in direct space, the NLCPA computational burden of repeated matrix inversions during effective medium construction grows instead as $O((N_c \times N_{\rm sub})^3)$, and can become more significant.

Upon having obtained a converged effective medium scattering path operator $\underline{\underline{\tau}}(z)$, deployment of Eqs. (6)–(8) present computational demands that grow with the number of cavity configurations $N_{\rm tot}$. The worst case scenario corresponds to a $SRO = 0$ statistics, for which all $N_{\rm tot} = \prod_{s=1}^{N_{\rm sub}} N_{alt}^{N_c}(s)$ possibilities should be considered. More generally, different kinds of local ordering are set up by altering the fully uncorrelated probability distribution given by a product of single-site concentrations alone. This typically leads to suppressing a large number of negligible contributions.

Evaluation of the remaining ones may be performed more efficiently and at no loss of accuracy by collecting into equivalence classes those configurations γ's which produce an equivalent impurity-projected scattering path operator from Eq. (5). This latter optimization has not proved crucial yet, due to limited complexity of examples considered so far.

[1] H. Ebert, S. Mankovsky, K. Chadova, S. Polesya, J. Minár, and D. Ködderitzsch, Calculating linear-response functions for finite temperatures on the basis of the alloy analogy model, Phys. Rev. B **91**, 165132 (2015).

[2] P. Soven, Coherent-potential model of substitutional disordered alloys, Phys. Rev. **156**, 809 (1967).

[3] Walter Metzner and Dieter Vollhardt, Correlated Lattice Fermions in $d = \infty$ Dimensions, Phys. Rev. Lett. **62**, 324 (1989).

[4] Antoine Georges, G. Kotliar, Werner Krauth, and M. J. Rozenberg, Dynamical mean-field theory of strongly correlated fermion systems and the limit of infinite dimensions, Rev. Mod. Phys. **68**, 13 (1996).

[5] P. Weinberger, *Electron Scattering Theory for Ordered and Disordered Matter* (Oxford University Press, Oxford, 1990).

[6] J. Zabloudil, R. Hammerling, L. Szunyogh, and P. Weinberger, *Electron scattering in solid matter* (Springer, Berlin, 2004).

[7] Hubert Ebert, D. Ködderitzsch, and J. Minár, Calculating condensed matter properties using the KKR-Green's function method–recent developments and applications, Rep. Prog. Phys. **74**, 096501 (2011).

[8] D. A. Rowlands, J. B. Staunton, and B. L. Györffy, The Korringa-Kohn-Rostoker Non-Local Coherent Potential Approximation (KKR-NLCPA), Phys. Rev. B **67**, 115109 (2003).

[9] Mark Jarrell, Th. Maier, C. Huscroft, and S. Moukouri, Quantum Monte Carlo algorithm for nonlocal corrections to the dynamical mean-field approximation, Phys. Rev. B **64**, 195130 (2001).

[10] Derwyn A. Rowlands, Short-range correlations in disordered systems: the Non-local Coherent-Potential Approximation, Psi-k newsletter **77**, 105 (2006).

[11] Derwyn A. Rowlands, Short-range correlations in disordered systems: nonlocal coherent-potential approximation, Rep. Prog. Phys. **72**, 086501 (2009).

[12] Derwyn A. Rowlands, Julie B. Staunton, Balazs Györffy, Ezio Bruno, and Beniamino Ginatempo, Effects of short-range order on the electronic structure of disordered metallic systems, Phys. Rev. B **72**, 045101 (2005).

[13] Derwyn A. Rowlands, Arthur Ernst, B. Györffy, and Julie B. Staunton, Density functional theory for disordered alloys with short-range order: Systematic inclusion of charge-correlation effects, Phys. Rev. B **73**, 165122 (2006).

[14] B. L. Györffy, G. M. Stocks, B. Ginatempo, Duane D. Johnson, D. M. Nicholson, F. J. Pinski, J. B. Staunton, H. Winter, H. Rafii-Tabar, J. B. Pendry, N. W. Ashcroft, V. Kumar, and L. M. Falicov, Order and Disorder in Metallic Alloys [and Discussion], Philos. Trans.: Phys. Sci. Eng. R. Soc. **334**, 515 (1991).

[15] D. A. Rowlands and Yu-Zhong Zhang, Dynamical nonlocal coherent-potential approximation for itinerant electron magnetism, J. Phys.: Condens. Matter **26**, 475602 (2014).

[16] Julie B. Staunton, Alberto Marmodoro, and Arthur Ernst, Using density functional theory to describe slowly varying fluctuations at finite temperatures: local magnetic moments in Gd and the 'not so local' moments of Ni, J. Phys.: Condens. Matter **26**, 274210 (2014).

[17] P. R. Tulip, Julie B. Staunton, S. Lowitzer, D. Ködderitzsch, and Hubert Ebert, Theory of electronic transport in random alloys with short-range order: Korringa-Kohn-Rostoker nonlocal coherent potential approximation, Phys. Rev. B **77**, 165116 (2008).

[18] S. Lowitzer, D. Ködderitzsch, Hubert Ebert, P. R. Tulip, Alberto Marmodoro, and Julie B. Staunton, An ab initio investigation of how residual resistivity can decrease when an alloy is deformed, Europhys. Lett. (Europhysics Letters) **92**, 37009 (2010).

[19] J. S. Faulkner and G. M. Stocks, Calculating properties with the coherent-potential approximation, Phys. Rev. B **21**, 3222 (1980).

[20] William H. Butler, Theory of electronic transport in random alloys: Korringa-Kohn-Rostoker coherent-potential approximation, Phys. Rev. B **31**, 3260 (1985).

[21] Julie B. Staunton, J. Poulter, and B. Ginatempo, Spin fluctuations in nearly magnetic metals from ab initio dynamical spin susceptibility calculations: Application to Pd and $Cr_{95}V_5$, Phys. Rev. B **62**, 1075 (2000).

[22] P. R. Tulip, Julie B. Staunton, Derwyn A. Rowlands, Balazs Györffy, Ezio Bruno, and B. Ginatempo, Nonsite diagonal properties from the Korringa-Kohn-Rostocker nonlocal coherent-potential approximation, Phys. Rev. B **73**, 205109 (2006).

[23] W. H. Butler and G. M. Stocks, Calculated electrical conductivity and thermopower of silver-palladium alloys, Phys. Rev. B **29**, 4217 (1984).

[24] Derwyn A. Rowlands, X.-G. Zhang, and Antonios Gonis, Reformulation of the nonlocal coherent-potential approximation as a unique reciprocal-space theory of disorder, Phys. Rev. B **78**, 115119 (2008).

[25] Alberto Marmodoro and Julie B. Staunton, Disorder in materials with complex crystal structures: the Non-Local Coherent Potential Approximation for compounds with multiple sublattices, J. Phys.: Conf. Ser. **286**, 012033 (2011).

[26] Alberto Marmodoro, Arthur Ernst, Sergei Ostanin, and Julie B. Staunton, Generalized inclusion of short-range ordering effects in the coherent potential approximation for complex-unit-cell materials, Phys. Rev. B **87**, 125115 (2013).

[27] A. J. Pindor, Julie B. Staunton, G. M. Stocks, and H. Winter, Disordered local moment state of magnetic transition metals: a self-consistent KKR CPA calculation, J. Phys. F **13**, 979 (1983).

[28] Julie Staunton, B. L. Györffy, A. Pindor, G. Stocks, and H. Winter, The "disordered local moment" picture of itinerant magnetism at finite temperatures, J. Magn. Magn. Mater. **45**, 15 (1984).

[29] H. Akai and P. H. Dederichs, Local moment disorder in ferromagnetic alloys, Phys. Rev. B **47**, 8739 (1993).

[30] J. B. Staunton, Relativistic effects and disordered local moments in magnets, Psi-k newsletter **82**, 88 (2007).

[31] E. Müller-Hartmann, Analyticity of the coherent potential approximation, Solid State Commun. **12**, 1269 (1973).

[32] G. M. Stocks, W. M. Temmerman, and B. L. Gyorffy, Complete Solution of the Korringa-Kohn-Rostoker Coherent-Potential-Approximation Equations: Cu-Ni Alloys, Phys. Rev. Lett. **41**, 339 (1978).

[33] E. Müller-Hartmann, Correlated fermions on a lattice in high dimensions, Zeitschrift für Physik B Condensed Matter **74**, 507 (1989).

[34] A. J. Pindor, W. M. Temmerman, and B. L. Györffy, KKR CPA for two atoms per unit cell: application to Pd and PdAg hydrides, J. Phys. F **13**, 1627 (1983).

[35] Melvin Lax, Multiple scattering of waves, Rev. Mod. Phys. **23**, 287 (1951).

[36] Melvin Lax, Multiple scattering of waves. II. The effective field in dense systems, Phys. Rev. **85**, 621 (1952).

[37] Stefan A. Maier, Jutta Ortloff, and Carsten Honerkamp, Dynamical cluster approximation with continuous lattice self-energy, Phys. Rev. B **88**, 235112 (2013).

[38] J. M. Cowley, An approximate theory of order in alloys, Phys. Rev. **77**, 669 (1950).

[39] J. M. Cowley, Short- and Long-Range Order Parameters in Disordered Solid Solutions, Phys. Rev. **120**, 1648 (1960).

[40] SCF-DFT calculations in this work have been typically performed resorting to a L(S)DA exchange-correlation kernel, in a scalar-relativistic description and making use of the atomic spheres approximation (ASA) for space filling. Ground state solutions have been generated with either the HUTSEPOT or SPR-KKR [7] multiple scattering codes.

[41] K. H. J. Buschow, P. G. van Engen, and R. Jongebreur, Magneto-optical properties of metallic ferromagnetic materials, J. Magn. Magn. Mater. **38**, 1 (1983).

[42] Ye. Palguyev, A. A. Kuranov, and Syutkin, Anomalous temperature dependence of the resistivity of ordering palladium-iron alloys, Phys. Met. Metallogr. **42**, 46 (1976) [Fiz. metal. metalloved. **42**, 57 (1976)].

[43] D. De Fontaine, The Cluster Variation Method and the Calculation of Alloy Phase Diagrams, edited by Malcolm G. Stocks and Antonios Gonis, in *Alloy Phase Stability*, Nato asi ed. (Kluwer Academic Publishers, Dordrecht, Boston, and London, 1989), pp. 177–203.

[44] Jürgen Kübler, *Theory of Itinerant Electron Magnetism* (Oxford University Press, Oxford, 2000).

[45] S. Lowitzer, D. Ködderitzsch, H. Ebert, and J. B. Staunton, Electronic transport in ferromagnetic alloys and the Slater-Pauling curve, Phys. Rev. B **79**, 115109 (2009).

[46] M. D. Watson, T. K. Kim, A. A. Haghighirad, N. R. Davies, A. McCollam, A. Narayanan, S. F. Blake, Y. L. Chen, S. Ghannadzadeh, A. J. Schofield, M. Hoesch, C. Meingast, T. Wolf, and A. I. Coldea, Emergence of the nematic electronic state in FeSe, Phys. Rev. B **91**, 155106 (2015).

[47] M. D. Watson, T. K. Kim, L. C. Rhodes, M. Eschrig, M. Hoesch, A. A. Haghighirad, and A. I. Coldea, Evidence for unidirectional nematic bond ordering in FeSe, Phys. Rev. B **94**, 201107(R) (2016).

[48] J. K. Glasbrenner, I. I. Mazin, Harald O. Jeschke, P. J. Hirschfeld, and Roser Valentí, Effect of magnetic frustration on nematicity and superconductivity in Fe chalcogenides, Nat. Phys. **11**, 953 (2015).

[49] Michael C. Gao, Jien-Wei Yeh, Peter K. Liaw, and Yong Zhang, editors, *High-Entropy Alloys* (Springer, Berlin, 2016).

[50] Fuyang Tian, Yang Wang, Douglas L Irving, and Levente Vitos, Applications of Coherent Potential Approximation to HEAs, in *High-Entropy Alloys* (Springer, Berlin, 2016), pp. 299–332.

[51] Aayush Sharma, Prashant Singh, Duane D. Johnson, Peter K. Liaw, and Ganesh Balasubramanian, Atomistic clustering-ordering and high-strain deformation of an $Al_{0.1}$CrCoFeNi high-entropy alloy, Sci. Rep. **6**, 31028 (2016).

[52] M. Claudia Troparevsky, James R. Morris, Paul R. C. Kent, Andrew R. Lupini, and G. Malcolm Stocks, Criteria for Predicting the Formation of Single-Phase High-Entropy Alloys, Phys. Rev. X **5**, 011041 (2015).

[53] M. Claudia Troparevsky, James R. Morris, Markus Daene, Yang Wang, Andrew R. Lupini, and G. Malcolm Stocks, Beyond Atomic Sizes and Hume-Rothery Rules: Understanding and Predicting High-Entropy Alloys, Jom **67**, 2350 (2015).